



TECHNICAL ARTICLE

# Effects of Solidification Conditions on Microstructure and Properties of High-Entropy Alloys from the CoCrFeMnNi Family

TOMASZ STASIAK <sup>1,3</sup> DARIUSZ OLESZAK<sup>2,4</sup>  
and ANNA FRACZKIEWICZ<sup>1,5</sup>

1.—Mines Saint-Etienne, CNRS, UMR 5307 LGF, Centre SMS, Univ Lyon, 42023 Saint-Etienne, France. 2.—Faculty of Materials Science and Engineering, Warsaw University of Technology, Woloska Str. 141, 02-507 Warsaw, Poland. 3.—e-mail: t.stasiak@yahoo.pl. 4.—e-mail: dariusz.oleszak@pw.edu.pl. 5.—e-mail: anna.fraczkiewicz@mines-stetienne.fr

Alloys from the CoCrFeMnNi family remain the most studied austenitic high-entropy alloys. In this study, four alloys, i.e., Cantor alloy, A3S (modified nonequiatom Cantor composition), both “pure” or doped with carbon (200 wt. ppm) and niobium (1.3 wt.%), were investigated. Firstly, alloys were induction cast using a cold-crucible method. The obtained ingots were molten, and rapidly solidified by melt-spinning at two cooling rates to obtain “ribbons”, typical of such processing. The effects of the solidification rate and the presence of carbon and niobium on the microstructure and hardness were studied. All the studied alloys show an fcc structure. The lattice parameter of the fcc phase increases with the increasing cooling rate, and with the addition of niobium and carbon, which confirms at least a partial presence of these elements in solid solution. Yet, TEM observations revealed the formation of nanometric NbC precipitates. The microstructure of melt-spun ribbons consists of equiaxed grains of a few micrometers in size. The higher cooling rate led to a small decrease in the grain size and a slight increase in hardness. Moreover, the hardness of doped alloys can be further improved by annealing (500°C for 24 h) through NbC precipitation.

## INTRODUCTION

High-entropy alloys (HEAs) are a quite new group of materials that have attracted high scientific and applicative interest since the first two publications by Cantor et al.<sup>1</sup> and Yeh et al.<sup>2</sup> In opposition to traditional alloys (steels, aluminum alloys, etc.), which contain only one or two main elements, HEAs are multicomponent alloys with at least five major components in concentrations, ideally, close to equiatomic ratios. Yeh et al.<sup>2,3</sup> proposed the name high-entropy alloys, based on the high mixing entropy due to the multielement composition, and introduced the four core effects (high entropy effect, sluggish diffusion, severe lattice distortion effect,

and cocktail effect) to explain their properties. Since then, the real importance of these effects on the behavior of HEAs has been frequently questioned.<sup>4,5</sup> The interesting debate on the four core effects and origins of HEA properties seems to be far from over.<sup>6</sup> Nevertheless, the large family of HEAs have attracted attention due to their outstanding properties: good mechanical properties at low<sup>7</sup> and high temperatures,<sup>8</sup> high creep resistance,<sup>9</sup> good weldability,<sup>10</sup> irradiation resistance,<sup>11</sup> and resistance to hydrogen embrittlement<sup>12</sup> and corrosion.<sup>13</sup>

The first discovered HEA, equiatomic CoCr-FeMnNi alloy, usually called Cantor alloy, is still the most studied. This alloy crystallizes in a single fcc phase; however, the decomposition of the fcc matrix and formation of the topologically close-packed  $\sigma$  phase and other complex phases occur after prolonged annealing between 500°C and 700°C.<sup>14,15</sup> The most characteristic properties of

(Received May 15, 2022; accepted September 20, 2022; published online October 6, 2022)

the Cantor alloy are an increase in yield strength and ductility with decreasing temperature, from room down to liquid nitrogen temperature, while the fracture toughness remains almost unchanged.<sup>7</sup> This behavior is attributed to the transition of the deformation mode from planar-slip dislocation to mechanical nanotwinning with decreasing temperature. The significant weakness of the Cantor alloy is its relatively poor mechanical resistance at room temperature.<sup>16</sup> In recent studies, some routes to strengthen the Cantor alloy have been presented, e.g., the doping by boron,<sup>17</sup> and the addition of carbon<sup>18,19</sup> or nitrogen.<sup>20</sup> Many articles have dealt with a strengthening by carbide precipitates, such as  $M_7C_3$ ,  $M_{23}C_6$ , etc.<sup>21,22</sup> NbC carbide seems to be particularly interesting, especially due to its high resistance to coarsening.<sup>23</sup> Studies of NbC strengthening of the Cantor alloy were published by Gao et al.<sup>24</sup> and Abbasi et al. in a series of articles.<sup>25–28</sup> NbC carbide is a very promising strengthening precipitate because it presents an fcc structure similar to the fcc phase in the Cantor HEA.<sup>24</sup> Yet, due to the low mobility of niobium atoms, strong segregation on Nb is currently observed in as-cast alloys. This phenomenon can lead to the presence of an NbC-containing eutectic mixture that solidifies at a temperature lower than the nominal melting temperature of the alloy, and consumes the major part of the niobium in an inefficient (from the point of view of precipitation hardening) way. However, the addition of niobium and carbon leads to a significant increase in hardness and tensile strength at room and higher temperatures, while the elongation is still relatively high.<sup>24,28</sup> Moreover, the presence of carbon and niobium can significantly reduce grain growth during homogenization annealing.<sup>25</sup> Besides strengthening, many papers have dealt with non-equiatom compositions of the Cantor alloy<sup>29,30</sup> with an addition of other elements, such as aluminum<sup>31</sup> or molybdenum.<sup>32</sup> One of the non-equiatom, so-called A3S, with the composition  $Co_{20}Cr_{15}Fe_{26}Mn_{17}Ni_{22}$ , was developed in the authors' laboratory.<sup>33,34</sup> It conserves the main assets of the Cantor alloy (low-temperature mechanical resistance) associated with improved stability of the fcc matrix at intermediate temperatures. For instance, after annealing at 500°C, no decomposition was observed for up to 300 days, while, for the equiatom alloy, the decomposition takes place after only 100 days.<sup>34</sup>

Melt-spinning is a rapid solidification technique in which a material is solidified from a liquid state by pouring it onto a moving refrigerated wheel; the obtained temperature gradient enables the reaching of a cooling rate of  $10^5$ – $10^7$  K s<sup>-1</sup>.<sup>35</sup> The precise cooling rate measurement during melt-spinning is very challenging; however, for a constant wheel diameter, it was found that the cooling rate increases linearly with increasing wheel speed.<sup>36</sup> To some extent, the structures produced by melt-spinning are similar to those obtained by additive

manufacturing processes; especially, fine grain size and limited solidification segregations can be expected.

Many HEAs have been prepared previously by melt-spinning.<sup>37–42</sup> The equiatom CoCrFeMnNi was fabricated in the first paper published by Cantor et al.<sup>1</sup> by rapid solidification. The completely crystalline alloy presents a single fcc phase with a lattice parameter close to the fcc iron. Another example of the melt-spun HEA is TiZrVCrNi, which consists of a single nanocrystalline Laves phase.<sup>39</sup> Some papers have discussed the magnetic properties<sup>38,40</sup> and corrosion resistance<sup>40</sup> of rapidly solidified alloys. Despite many articles dealing with HEAs prepared by melt-spinning, there is a lack of papers discussing the effects of the cooling rate and the addition of carbon on the microstructure and mechanical properties of materials elaborated by this technique.

In this study, the elaboration of HEAs from the CoCrFeMnNi family by rapid solidification via melt-spinning was investigated. The effects of the cooling rate and the addition of niobium and carbon on the microstructure and hardness of equiatom and non-equiatom Cantor alloys were studied. The solidification segregations and the possibility of the formation of nanometric NbC carbides and their role in the hardness evolution were also analyzed.

## EXPERIMENTAL

### Materials

In this study, four alloys have been analyzed: equiatom CoCrFeMnNi (Cantor alloy, internal reference: “E” from equiatom), a modified composition from the Co-Cr-Fe-Mn-Ni system (referenced as “N” from nonequiatom<sup>33</sup>), and both alloys with the addition of niobium and carbon (referenced by “D” letter following the alloy denomination). The chemical composition of the alloys is shown in Table I. Firstly, the alloys were cast by induction melting in a cold crucible, starting from high-purity raw materials (C, N, O level below 20 wt. ppm each). The obtained ingots (250 g each) were molten and rapidly solidified by melt-spinning (Melt Spinner HV; Edmund Bühler) at 200 mbar argon pressure at two cooling rates: 20 and 70 rotations of the copper wheel per second, which is equivalent to a linear wheel speed of 16 m/s and 55 m/s, respectively. Selected melt-spun ribbons were annealed at 500°C and 600°C for 24 h under vacuum-sealed tubes, and then cooled slowly in tubes outside the furnace.

### Materials Characterization

The structure, microstructure, and microhardness of the melt-spun ribbons were investigated in this study. The crystal structure of the ribbons was examined by x-ray diffraction (XRD) using a Bruker D8 Advance x-ray diffractometer with a Cu K $\alpha$  radiation source ( $\lambda = 1.5418$  Å). The scanning step

**Table I. Chemical composition (wt.%) of the investigated alloys**

Alloy/element	Fe	Cr	Ni	Mn	Co	C	Nb
E-D	19.18	18.40	20.80	19.50	20.80	0.02	1.30
E	19.90	18.50	21.00	19.60	21.00	–	–
N-D	24.98	13.70	22.70	16.40	20.90	0.02	1.30
N	25.80	13.80	22.90	16.60	20.90	–	–

*E, N* denomination of the alloys; see text for details. *D* doped (containing Nb and C) alloys, in contrast to the pure alloys.

was  $0.02^\circ$  from  $2\theta = 10^\circ$  to  $100^\circ$  with a time step of 5 s. For scanning electron microscopy (SEM) and electron backscatter diffraction (EBSD) analyses, the samples were cold-mounted, then manually polished with SiC grinding papers (P320–P4000), and finally polished by Struers LectroPol-5, using an electropolishing bath of 6% perchloric acid ( $\text{HClO}_4$ ) and ethanol ( $\text{C}_2\text{H}_5\text{OH}$ ) with an applied voltage between 18 V and 25 V for a few seconds. Besides the preparation of the appropriate surface for the microscopic investigations, the polishing led to the removal of a considerable thickness, and thus allowed the observation of the microstructure between the air and the wheel side of the ribbons. The SEM observations were performed using a Zeiss Supra 55 VP SEM operated at 20 kV equipped with energy-dispersive x-ray spectroscopy (EDX) and EBSD detectors. The grain size measurements were carried out using the linear intercept method based on the SEM-BSE images of at least 200 grains for each sample. The EBSD data were obtained with a step size between 40 nm and 80 nm, and analyzed by HKL Channel5 software. Transmission electron microscope (TEM) observations were carried out using a Philips CM200 TEM equipped with an EDX detector operated at 200 kV. The TEM samples were prepared by conventional twinjet electropolishing. Discs with a diameter of about 3 mm were cut from the ribbons, slightly polished on both sides, and then electropolished using a Struers TenuPol-5 with a solution of 10% perchloric acid in ethanol at a 15 V potential at temperatures between  $-2^\circ\text{C}$  and  $-5^\circ\text{C}$ . The samples for microhardness analysis were prepared similarly to those for the SEM investigation except for the electropolishing. Microhardness was measured using a Matsuzawa Microhardness Tester MX T70 under a load of 10 g with a dwell time of 10 s. For each sample, at least ten indents were made.

## RESULTS AND DISCUSSION

### Macroscopic Observations

The alloys prepared by melt-spinning were in the form of ribbons, which is common for non-brittle metallic materials produced by this technique.<sup>35,36</sup> The macroscopic observations of the samples

showed that the cooling rate (20 R or 70 R) significantly affects the size of the ribbons (Fig. 1). The length, thickness, and width of the ribbons decrease with an increasing cooling rate. The width decreases from about 3 mm at 20 R to about 1.5 mm at 70 R. The length varies significantly between each ribbon; however, a general decrease with an increasing cooling rate can be observed. The most important feature seems to be a decrease in thickness from  $90\ \mu\text{m}$  at 20 R to  $70\ \mu\text{m}$  at 70 R. Tkatch et al.<sup>43</sup> and Gheiratmand et al.<sup>44</sup> found a reduction in the thickness of melt-spun ribbons with an increasing cooling rate (wheel velocity). A higher wheel velocity also enhances the heat transfer (ribbon–wheel interface), which increases the cooling rate.<sup>36,43</sup> The size of the ribbons produced in this study seemed to be independent of the chemical composition of the alloys and comparable to other HEAs produced by melt-spinning.<sup>37</sup> The roughness (not quantified) seems higher on the free-side than on the wheel-side of the ribbons. Roughness can be caused by the gaseous atmosphere in the chamber.<sup>45</sup>

### Crystal Structure

The XRD results (refer to online supplementary material, Fig. S-1) revealed that all the samples presented an austenitic crystal structure (fcc,  $a = 3.59\text{--}3.60\ \text{\AA}$ ). This is in good agreement with other experimental and theoretical studies that the Cantor alloy could not be vitrified via melt-spinning and presents a single fcc structure after preparation by this technique.<sup>1,46</sup> No other phases, e.g., NbC precipitates, were present in the doped samples as examined by XRD, which will be related to the low volume fractions of possible phases. The effect of cooling rate on lattice parameters was observed, i.e., the samples prepared at 70 R presented a slightly larger lattice parameter than samples prepared at 20 R (Fig. 2a). Similar to other studies,<sup>26,28</sup> the addition of niobium and carbon causes an increase in lattice parameters in both alloys. The fcc lattice could accommodate alloying elements, which results in an increase in the lattice parameter.<sup>27,28</sup> This is consistent with other studies evaluating the addition of carbon to the Cantor alloy. Stepanov et al.<sup>18</sup> found that the lattice parameter of the Cantor alloy increases by  $0.0065\ \text{\AA}$  per 1 at.% (or 0.2 wt.%) of



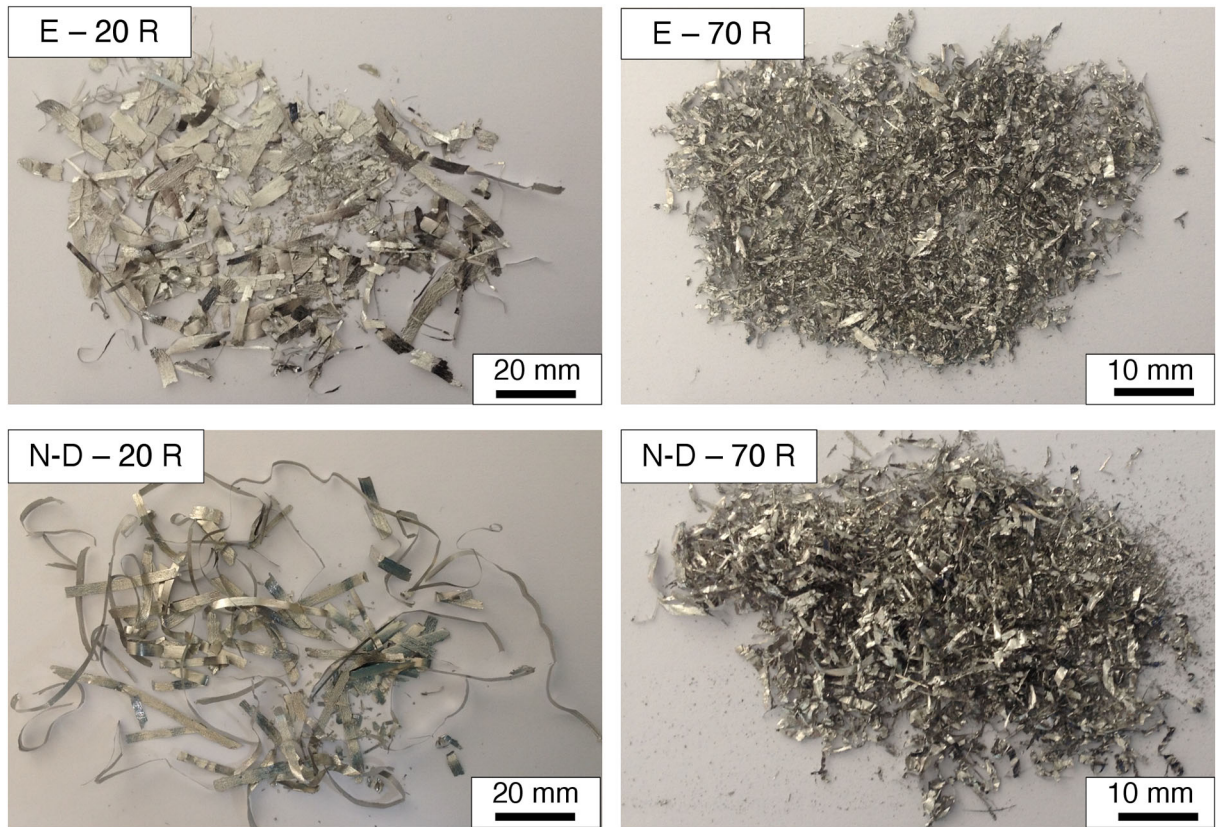


Fig. 1. Images of selected ribbons obtained by melt-spinning.

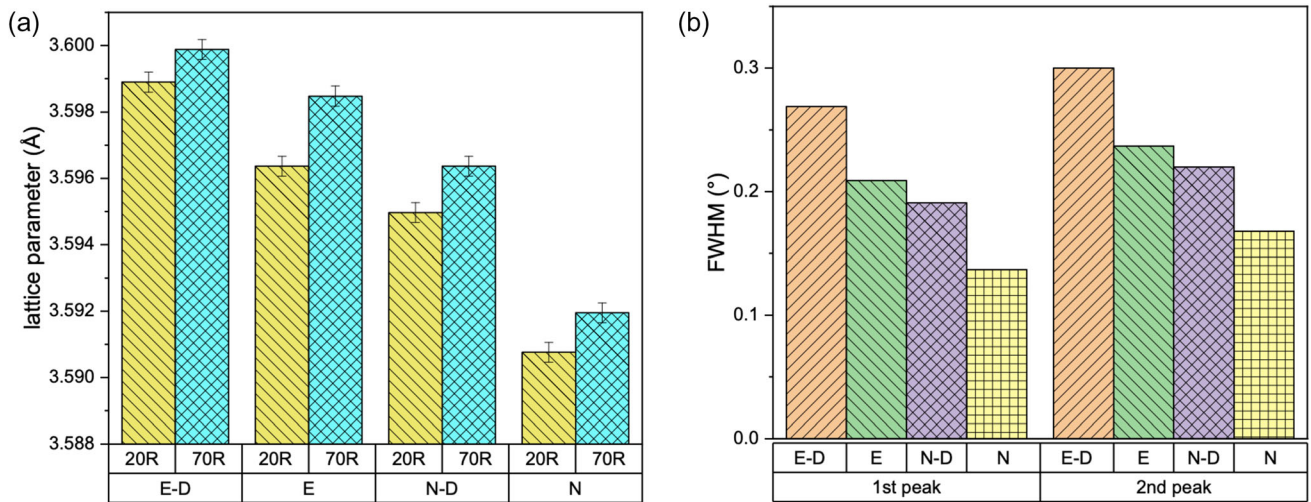


Fig. 2. Lattice parameters of studied alloys (a) and the full width of half-maximum (FWHM) of two first peaks ((111) and (200)) of melt-spun ribbons prepared at 20 R (b).

carbon. The addition of carbon in this study was 0.02 wt.% (0.1 at.%); however, the increase of the lattice parameter is about 0.0025 Å for E and 0.0042 Å for N alloy. Therefore, the increase of the lattice parameter should also be related to the niobium addition and its dissolution in the fcc phase. It should also be noted that the lattice parameter of N alloy is slightly lower than that of

E alloy, which was also confirmed in an as-forged state in a previous study in the authors' laboratory.<sup>35</sup> This could be a result of a smaller atomic radius difference in N than in E. The calculation of the lattice parameters by Vegard's law, using similar lattice constants of pure elements as in a study by Laurent-Brocq et al.,<sup>47</sup> confirms a smaller lattice parameter for N alloy than for the equiatomic

alloy. The analyses of the full width of half-maximum (FWHM) of the two first peaks ((111) and (200)) showed the effects of chemical composition (E versus N) and the addition of carbon and niobium on this parameter (Fig. 2b). The N and N-D present smaller FWHMs than E and E-D, respectively. Moreover, alloys doped with niobium and carbon present slightly larger FWHMs than pure alloys, which could result from a smaller crystallite size and higher lattice strain in alloys with the addition of niobium and carbon.

### Microstructure

The SEM observations showed that the microstructure of all the examined melt-spun samples consisted of equiaxed grains without any twin boundaries (Fig. 3, and Supplementary material, Fig. S-2). This is in opposition to the as-cast alloys, which present a dendritic structure (overall chemical composition is close to the initial one), i.e., the segregation of manganese and nickel to interdendritic areas and regions rich in niobium (Supplementary material, Fig. S-3). This is consistent with the literature that an alloy can present a dendritic microstructure after casting (slow cooling rate) and equiaxed, fine grains after melt-spinning.<sup>40</sup> The average grain size in the melt-spun samples was from about 2.1 up to 5.7  $\mu\text{m}$  (Fig. 4). However, Chattopadhyay et al.<sup>46</sup> found a slightly smaller

grain size (about 1  $\mu\text{m}$ ) in the melt-spun ribbons (40 m/s linear wheel speed) of the Cantor alloy. Nevertheless, the results in this study are in reasonable agreement with the findings by Chattopadhyay et al.<sup>46</sup> The ribbons prepared at 20 R present roughly a similar grain size regardless of chemical composition. The samples cooled at 70 R consist of smaller grains, which is related to a faster cooling rate at a higher rotation speed. Moreover, ribbons cooled at 70 R doped with niobium and carbon (especially E-D) present a significantly smaller grain size than pure alloys. The pores visible in all the SEM-BSE images in Fig. 3 are related to the preparation of samples for microscopic observations using electropolishing. The chemical composition of the melt-spun ribbons is similar to the initial compositions listed in Table I. The distribution of the metallic elements is rather homogeneous at the SEM scale (Supplementary material, Fig. S-4) in all the melt-spun ribbons, except for the presence of micrometric niobium-rich precipitates in the doped alloys (Supplementary material, Fig. S-5) and very small segregations. It should be noted that small segregations (manganese and nickel to interdendritic regions and other main elements to dendritic areas) barely visible at the SEM-EDX scale were observed inside the equiaxed grains, mainly in the melt-spun samples without the addition of niobium and carbon (Fig. 3a and b). The size of the segregations is much smaller than in

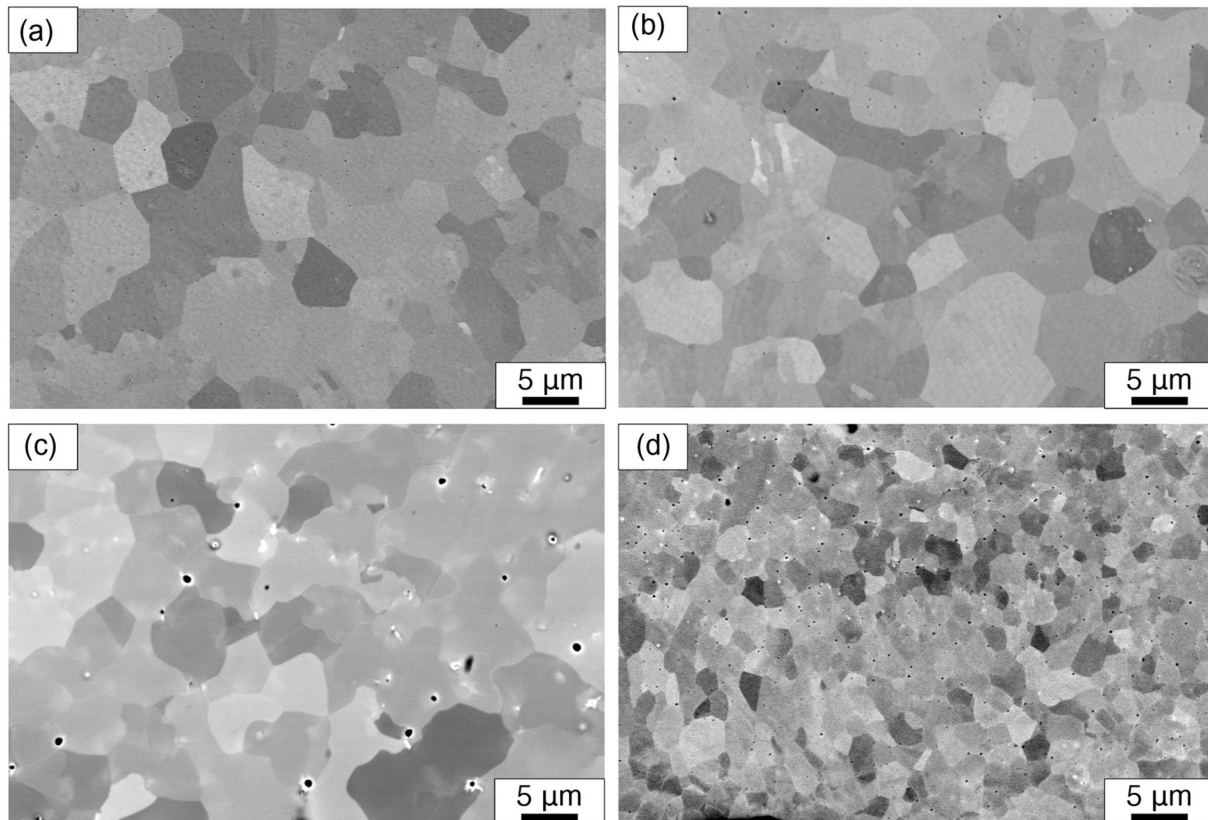


Fig. 3. SEM-BSE images of the microstructure of selected melt-spun ribbons: (a) E-20 R, (b) E-70 R, (c) E-D-20 R, and (d) E-D-70 R.



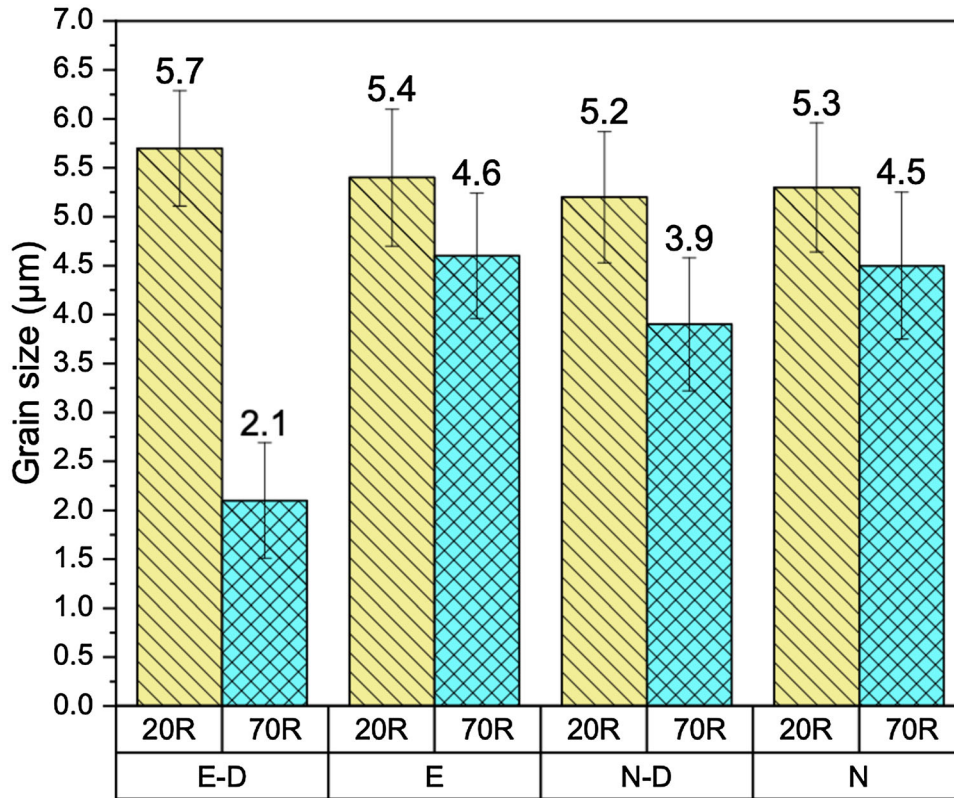


Fig. 4. Grain size measured in melt-spun ribbons.

the dendritic as-cast structure, so it could not even be compared with the as-cast structure.

EBSD analyses (Fig. 5) confirmed a similar grain size as measured by the linear intercept method from the SEM-BSE images. EBSD inverse pole figure maps showed uniform orientation inside the

grains, i.e., no subgrain formation, in all the studied samples. Conclusions about the differences in the texture strengths among the produced samples based on the EBSD results cannot be made because of the relatively small number of grains analyzed by the EBSD technique. However, the XRD results

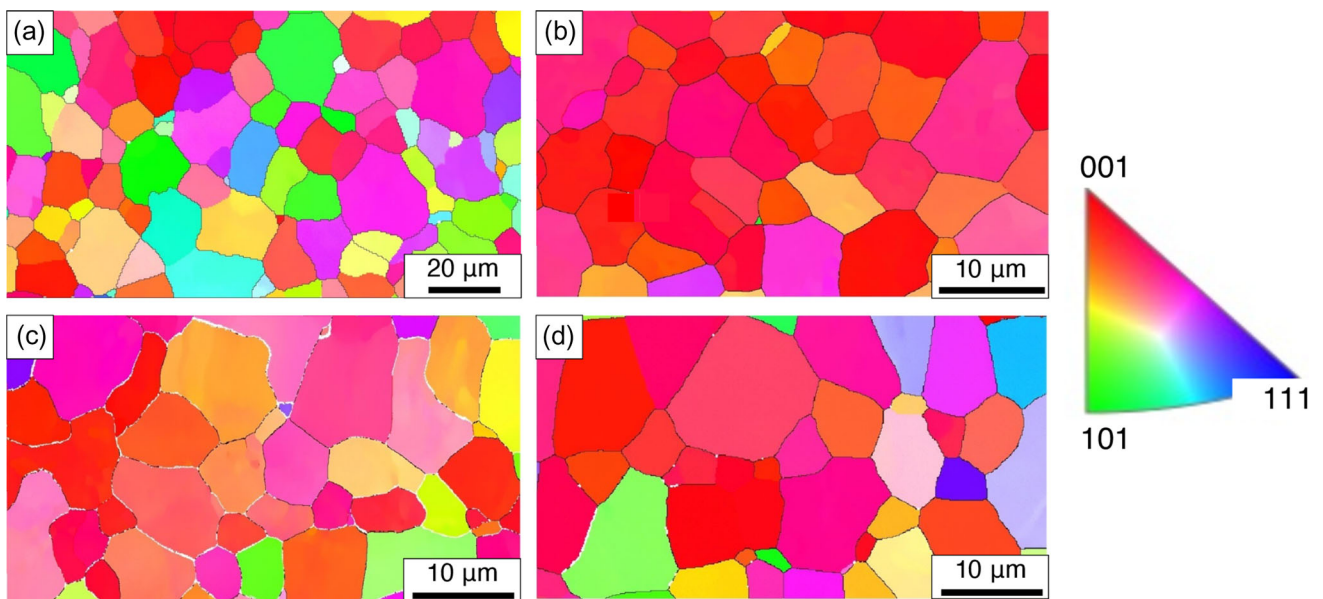


Fig. 5. EBSD inverse pole figure maps of melt-spun ribbons prepared with rotation of 20 R: (a) E-D-20 R, (b) E-20 R, (c) N-D-20 R, and (d) N-20 R alloys.

(Supplementary material, Fig. S-1) show that none of the produced ribbons revealed any texture. No twin boundaries currently observed in deformed and annealed (recrystallized) bulk alloys from the CoCrFeMnNi family<sup>34,48</sup> were present in the melt-spun ribbons.

TEM observations (Fig. 6) revealed equiaxed grains of the size of a few micrometers, which is in good agreement with the SEM and EBSD results. Besides grain size, no significant differences in terms of microstructure between the samples were detected at low magnification. A relatively high dislocation density (estimated to be between  $10^{13} \text{ m}^{-2}$  and  $10^{14} \text{ m}^{-2}$ ) was detected, which is roughly comparable to the as-forged state,<sup>34</sup> and seems to be lower in the vicinity of grain boundaries than inside the grains. The high dislocation density ( $5.7 \times 10^{13}$ – $1.3 \times 10^{14} \text{ m}^{-2}$ ) has been previously reported in melt-spun alloys.<sup>49,50</sup> Lin et al.<sup>49</sup> explained the high dislocation density by a very short timeframe during rapid solidification for atoms to arrange from the completely disordered state in liquid to form a crystal structure in the solid state. This rapid arrangement would lead to the creation of crystal defects, mainly in the form of dislocations. Higher magnification TEM observations revealed precipitates in the doped alloys (Fig. 7). These randomly distributed precipitates were identified as NbC (fcc structure, lattice parameter 4.47 Å). The precipitates were nanometric with a size between 10 nm and 20 nm. The nanoscale NbC precipitates were found in other studies in the Cantor alloy prepared by different methods.<sup>24</sup> The precipitates should have a substantial effect on the strength of the alloy. No other types of carbides

were found. According to the study by Powell et al.,<sup>51</sup> when the ratio of niobium to carbon in weight percent is below 7.7, both NbC and  $\text{M}_{23}\text{C}_6$  could be formed in austenitic steels, while, for a ratio greater than 7.7, the NbC formation is privileged. In the studied alloys (E-D, N-D), this ratio is 65, so the content of niobium is largely sufficient to combine with carbon to form NbC without the simultaneous formation of other carbides. It is important to note that the small size of all the NbC particles shows their formation in the solid state during the material's cooling. Thus, these results show that the currently observed significant solidification segregation and the presence of eutectic carbides could be avoided, thanks to the high solidification rate during the melt-spinning process.

### Microhardness Results

The microhardness of the melt-spun ribbons results from different strengthening mechanisms, i.e., solid-solution hardening, grain boundary hardening, dislocation (strain) hardening, and precipitation hardening. It can be assumed that, despite different compositions of the studied samples, the contribution of solid-solution hardening is roughly similar. The microhardness of ribbons showed that alloys doped with carbon and niobium present slightly higher hardnesses than their pure counterparts (Fig. 8a). It is the effect of the presence of nanometric NbC precipitates which can impede movements of dislocations in E-D and N-D alloys. The increase of hardness and strength by the formation of NbC precipitates in the Cantor alloy has already been reported in the literature.<sup>24,27</sup> The

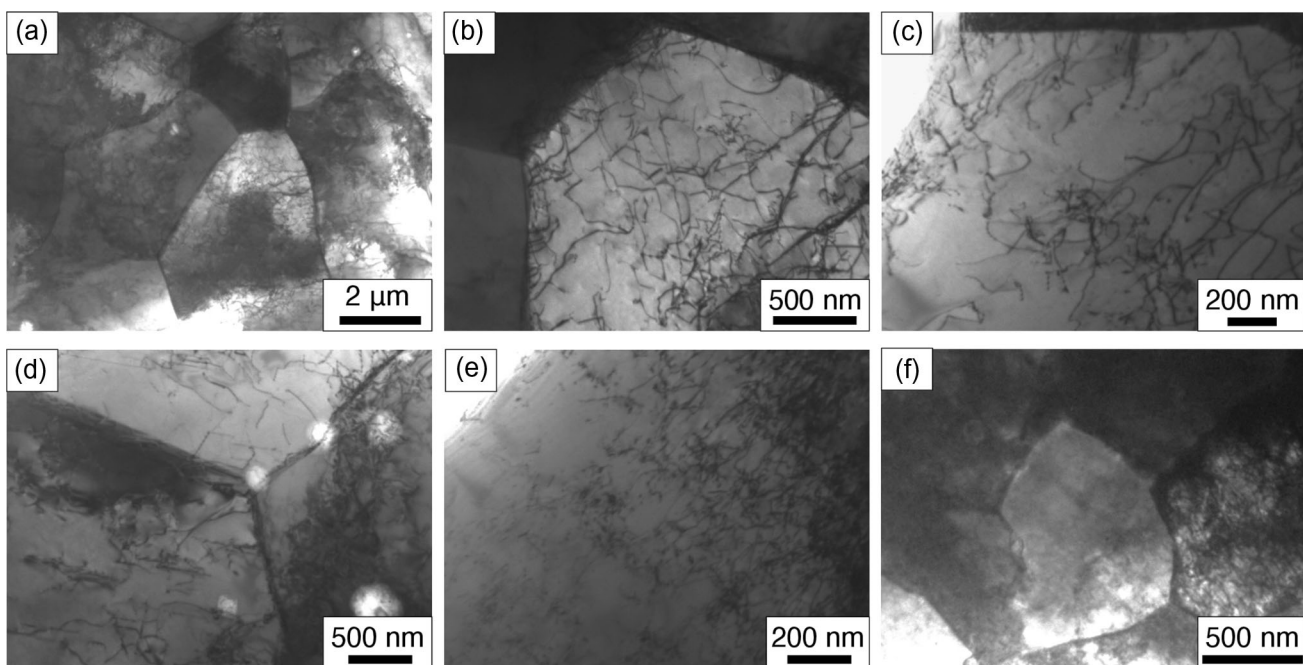


Fig. 6. TEM bright field images of microstructure: (a) E-20 R (low magnification), (b) E-20 R (higher magnification), (c) N-D-20 R, (d) N-20 R, (e) E-70 R, (f) N-D-70 R.

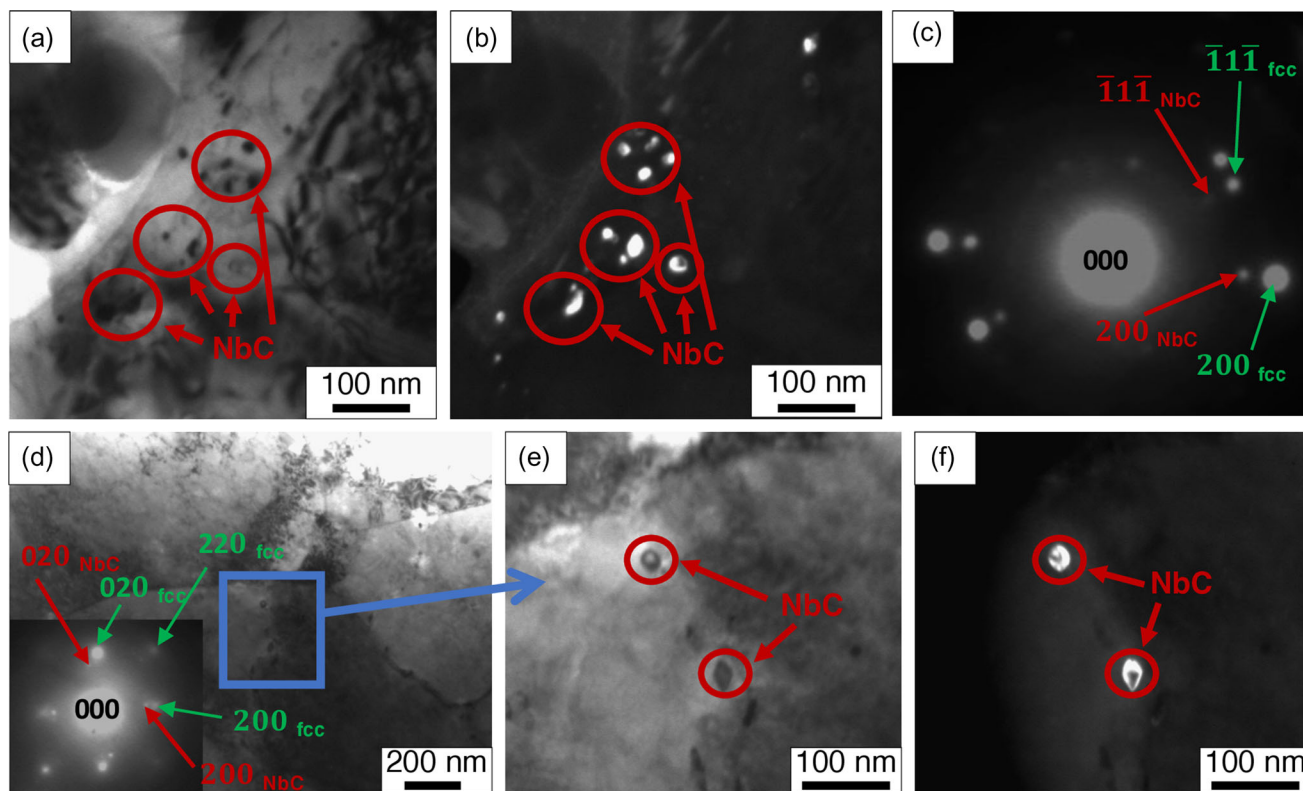


Fig. 7. TEM images of NbC carbide precipitates: (a) and (b) bright and dark (taken with  $[200]$  spot of NbC) field images, respectively, showing nanometric NbC precipitates in E-D-70 R; (c) selected area diffraction of the zone shown in (a) and (b), zone axis (fcc) near  $\langle 011 \rangle$ ; (d) bright field image with selected area diffraction revealing nanometric NbC precipitates in N-D-70 R, zone axis (fcc)  $\langle 001 \rangle$ ; (e) and (f) higher magnification bright and dark (taken with  $[020]$  spot of NbC) field images, respectively, showing nanometric precipitates.

cooling rate also plays a role in microhardness. The alloys prepared at 70 R present higher microhardness than alloys that were cooled slightly more slowly (20 R). This is mainly the effect of smaller grain size in faster-solidified alloys (Fig. 4), and probably a higher dislocation density due to a shorter timeframe for atoms to arrange from a liquid state to a crystal structure. However, the grain boundary strengthening is not very powerful, because, for sample E-D, the grain size decreases by  $3.6 \mu\text{m}$  between 20 R and 70 R, while the hardness increases by only 17 HV.

The microhardness of ribbons prepared at 20 R and 70 R was also measured after annealing for 24 h at  $500^\circ\text{C}$  and  $600^\circ\text{C}$  (Fig. 8b and c). For alloys without the addition of niobium and carbon, the microhardness decreases are almost constant after annealing due to grain growth and recovery. The microhardness of doped alloys increases after annealing at  $500^\circ\text{C}$ , e.g., from  $238 \text{HV}_{0.01}$  to  $263 \text{HV}_{0.01}$  for the E-D-20 R alloy. After annealing at  $600^\circ\text{C}$ , the hardness decreases (more significantly for the N-D alloy) compared to the heat treatment results at  $500^\circ\text{C}$ . Nevertheless, it should be noted that the hardness is slightly higher than in the as-spun state. The hardening of the doped alloys is the effect of the formation of additional NbC carbides during annealing (precipitation hardening). The

precipitation of these carbides overcomes the grain growth and recovery occurring during heat treatment (Fig. 8d). The high density of dislocations in melt-spun ribbons could be beneficial in the formation of nanoprecipitates because defects can act as nucleation sites.<sup>27,52</sup> The microstructure was observed by SEM-BSE after annealing (Fig. 9). The grain growth in the E-D alloy seems more important than in the N-D alloy, and is in good agreement with previous studies.<sup>34</sup>

## CONCLUSION

Alloys from the CoCrFeMnNi family were prepared by melt-spinning. The effects of the solidification rate and the addition of carbon and niobium on the structure, microstructure, and microhardness were studied.

1. All the samples prepared by rapid solidification presented an austenitic (fcc) structure without any presence of an amorphous phase. A higher cooling rate caused a slight increase in the lattice parameter. Doping with carbon and niobium also increased the lattice parameter of both alloys, and therefore it revealed that some fractions of these elements are in the solid solution. Peak width (FWHM) was larger for a higher cooling rate, which confirms that alloys



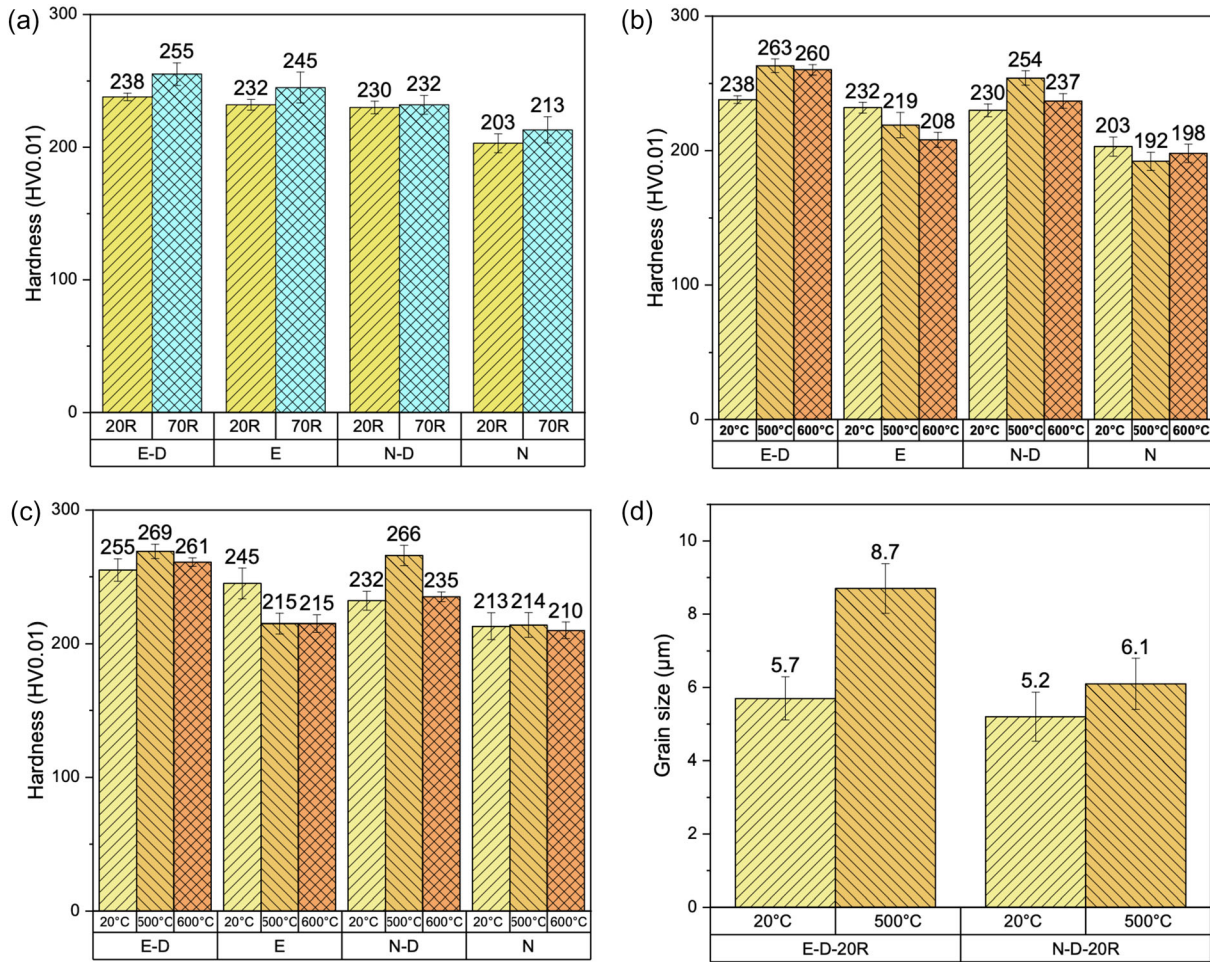


Fig. 8. Hardness and grain size measurements: (a) hardness of melt-spun ribbons, (b) hardness of annealed melt-spun ribbons prepared with rotation of 20 R, (c) hardness of annealed melt-spun ribbons prepared with rotation of 70 R, (d) comparison of grain size of melt-spun ribbons before and after annealing. The temperature values correspond to the annealing temperature.

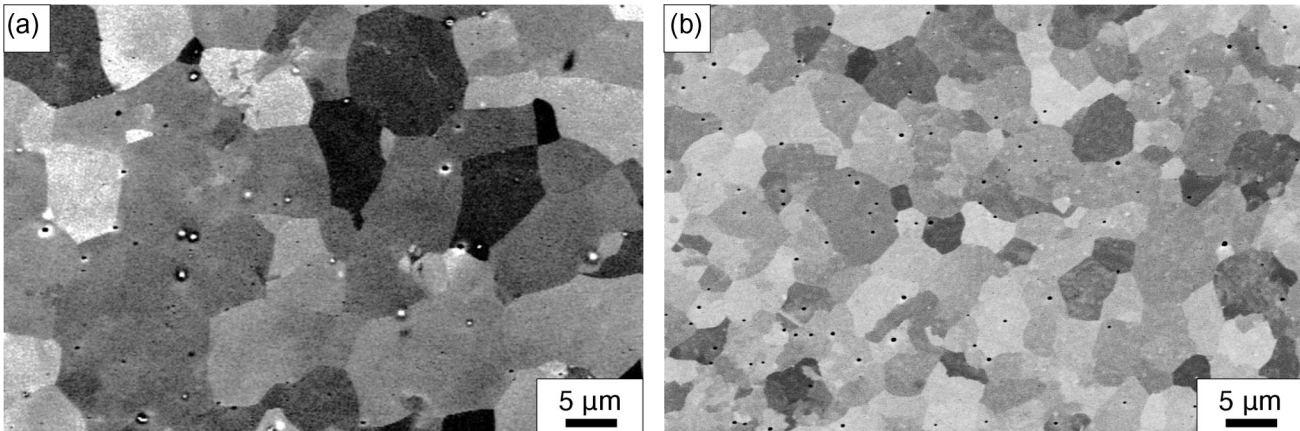


Fig. 9. SEM-BSE images of melt-spun ribbons after annealing at 500°C for 24 h: (a) E-D-20 R and (b) N-D-20 R.

are better crystallized at a lower solidification rate.

- Melt-spun ribbons consist of a fine-grained microstructure of equiaxed grains. The grain size is about a few micrometers and is decreases

slightly with an increasing cooling rate. The grains present a relatively high dislocation density (estimated between  $10^{13} \text{ m}^{-2}$  and  $10^{14} \text{ m}^{-2}$ ). The orientation inside the grains is almost homogenous; no presence of subgrains

was detected. Nanometric NbC precipitates (10–20 nm) were detected in doped alloys.

- The microhardness slightly increases for the higher cooling rate, which could be mainly related to the smaller grain size. As-spun ribbons with the addition of carbon and niobium presented a slightly higher microhardness than the pure alloy, which is the effect of the nanometric NbC precipitates. Further increases of microhardness of the doped alloys could be achieved through annealing at 500°C for 24 h. Such heat treatment causes precipitation from the solid solution of more NbC precipitates.
- No harmful NbC-containing eutectic mixture solidifying at low temperatures at the end of solidification was observed. It was shown that the cooling rates obtained in the melt-spinning process are high enough to retain niobium atoms in solid solution in the matrix, and make them available for precipitation hardening in selected thermal conditions of annealing.

## SUPPLEMENTARY INFORMATION

The online version contains supplementary material available at <https://doi.org/10.1007/s11837-022-05543-2>.

## ACKNOWLEDGEMENTS

The authors would like to acknowledge the late Dr. Jerzy Latuch (WUT) for the preparation of alloys by melt-spinning. The authors gratefully thank the staff from the MINES lab: Olivier Valfort (XRD analyses), Claude Varillon (alloys elaboration), Gilles Blanc (metallographic preparation of samples), and Delphine Juhem (samples preparation for TEM analyses).

## CONFLICT OF INTEREST

The authors declare that they have no known competing financial interests or personal relationships that could have appeared to influence the work reported in this paper.

## REFERENCES

- B. Cantor, I.T.H. Chang, P. Knight, and A.J.B. Vincent, *Mater. Sci. Eng. A* 375–377, 213 (2004).
- J.-W. Yeh, S.-K. Chen, S.-J. Lin, J.-Y. Gan, T.-S. Chin, T.-T. Shun, C.-H. Tsau, and S.-Y. Chang, *Adv. Eng. Mater.* 6, 299 (2004).
- J.-W. Yeh, *Ann. Chim. Sci. Mater.* 31, 633 (2006).
- D.B. Miracle, and O.N. Senkov, *Acta Mater.* 122, 448 (2017).
- J. Dąbrowa, M. Zajusz, W. Kucza, G. Cieślak, K. Berent, T. Czeppe, T. Kulik, and M. Danielewski, *J. Alloys Compd.* 783, 193 (2019).
- K. Biswas, J.W. Yeh, P.P. Bhattacharjee, and J.T.M. DeHosson, *Scr. Mater.* 188, 54 (2020).

- B. Gludovatz, D. Catoor, E.H. Chang, A. Hohenwarter, E.P. George, and R.O. Ritchie, *Science (80-)* 345, 1153 (2014).
- O.N. Senkov, G.B. Wilks, J.M. Scott, and D.B. Miracle, *Intermetallics* 19, 698 (2011).
- T.K. Tsao, A.C. Yeh, C.M. Kuo, K. Takehi, H. Murakami, J.W. Yeh, and S.R. Jian, *Sci. Rep.* 7, 1 (2017).
- S.S. Nene, K. Liu, M. Frank, R.S. Mishra, R.E. Brennan, K.C. Cho, Z. Li, and D. Raabe, *Sci. Rep.* 7, 16167 (2017).
- O. El-Atwani, N. Li, M. Li, A. Devaraj, J.K.S. Baldwin, M.M. Schneider, D. Sobieraj, J.S. Wróbel, D. Nguyen-Manh, S.A. Maloy, and E. Martinez, *Sci. Adv.* 5, eaav2002 (2019).
- H. Luo, W. Lu, X. Fang, D. Ponge, Z. Li, and D. Raabe, *Mater. Today* 21, 1003 (2018).
- Y. Shi, B. Yang, X. Xie, J. Brechtel, K.A. Dahmen, and P.K. Liaw, *Corros. Sci.* 119, 33 (2017).
- F. Otto, A. Dlouhý, K.G. Pradeep, M. Kuběnová, D. Raabe, G. Eggeler, and E.P. George, *Acta Mater.* 112, 40 (2016).
- E.J. Pickering, R. Muñoz-Moreno, H.J. Stone, and N.G. Jones, *Scr. Mater.* 113, 106 (2016).
- B. Cantor, *Prog. Mater. Sci.* 120, 100754 (2020).
- J.B. Seol, J.W. Bae, Z. Li, J. Chan Han, J.G. Kim, D. Raabe, and H.S. Kim, *Acta Mater.* 151, 366 (2018).
- N.D. Stepanov, N.Y. Yurchenko, M.A. Tikhonovskiy, and G.A. Salishchev, *J. Alloys Compd.* 687, 59 (2016).
- J. Li, B. Gao, Y. Wang, X. Chen, Y. Xin, S. Tang, B. Liu, Y. Liu, and M. Song, *J. Alloys Compd.* 792, 170 (2019).
- K.S. Chung, P.M. Yiu, T.F. Hung, and C.H. Shek, *J. Alloys Compd.* 871, 159587 (2021).
- J.Y. Ko, and S.I. Hong, *J. Alloys Compd.* 743, 115 (2018).
- H. Cheng, H.Y. Wang, Y.C. Xie, Q.H. Tang, and P.Q. Dai, *Mater. Sci. Technol.* 33, 2032 (2017).
- C. Scott, B. Remy, J.L. Collet, A. Cael, C. Bao, F. Danoix, B. Malardc, and C. Curfse, *Int. J. Mater. Res.* 102, 538 (2011).
- N. Gao, D.H. Lu, Y.Y. Zhao, X.W. Liu, G.H. Liu, Y. Wu, G. Liu, Z.T. Fan, Z.P. Lu, and E.P. George, *J. Alloys Compd.* 792, 1028 (2019).
- E. Abbasi, and K. Dehghani, *Mater. Sci. Eng. A* 753, 224 (2019).
- E. Abbasi, and K. Dehghani, *J. Alloys Compd.* 783, 292 (2019).
- E. Abbasi, and K. Dehghani, *Mater. Sci. Eng. A* 772, 138812 (2020). <https://doi.org/10.1016/j.msea.2019.138812>.
- E. Abbasi, and K. Dehghani, *Mater. Sci. Eng. A* 772, 138771 (2020). <https://doi.org/10.1016/j.msea.2019.138771>.
- G. Bracq, M. Laurent-Brocq, C. Varvenne, L. Perrière, W.A. Curtin, J.M. Joubert, and I. Guillot, *Acta Mater.* 177, 266 (2019).
- S.F. Liu, Y. Wu, H.T. Wang, J.Y. He, J.B. Liu, C.X. Chen, X.J. Liu, H. Wang, and Z.P. Lu, *Intermetallics* 93, 269 (2018).
- J.Y. He, W.H. Liu, H. Wang, Y. Wu, X.J. Liu, T.G. Nieh, and Z.P. Lu, *Acta Mater.* 62, 105 (2014).
- G. Qin, R. Chen, H. Zheng, H. Fang, L. Wang, Y. Su, J. Guo, and H. Fu, *J. Mater. Sci. Technol.* 35, 578 (2019).
- A. Fraczkiewicz, French Patent, FR-1459567 (2014).
- M. Mroz, *Design and Structural Optimization of a High Entropy Alloy (HEA) of the CoCrFeMnNi Family with High Mechanical Resistance*, Ph.D. thesis, Ecole des Mines de Saint Etienne, France (2018).
- E.J. Lavernia, and T.S. Srivatsan, *J. Mater. Sci.* 45, 287 (2010).
- A.G. Gillen, and B. Cantor, *Acta Metall.* 33, 1813 (1985).
- J. Rogal, F. Morgiel, B.B. Stein, and J. Dutkiewicz, *Mater. Charact.* 148, 134 (2019).
- C. Chen, H. Zhang, Y. Fan, W. Zhang, R. Wei, T. Wang, T. Zhang, and F. Li, *J. Magn. Magn. Mater.* 502, 166513 (2020).
- T.P. Yadav, S. Mukhopadhyay, S.S. Mishra, N.K. Mukhopadhyay, and O.N. Srivastava, *Philos. Mag. Lett.* 97, 494 (2017).
- C. Chen, H. Zhang, Y. Fan, R. Wei, W. Zhang, T. Wang, T. Zhang, K. Wu, F. Li, S. Guan, and J. Jiang, *Intermetallics* 122, 106778 (2020).

41. Q. Hu, S. Guo, J.M. Wang, Y.H. Yan, S.S. Chen, D.P. Lu, K.M. Liu, J.Z. Zou, and X.R. Zeng, *Sci. Rep.* 7, 1 (2017).
42. B. Sarac, V. Zadorozhnyy, E. Berdonosova, Y.P. Ivanov, S. Klyamkin, S. Gumrukcu, A.S. Sarac, A. Korol, D. Semenov, M. Zadorozhnyy, A. Sharma, A.L. Greer, and J. Eckert, *RSC Adv.* 10, 24613 (2020).
43. V.I. Tkatch, A.I. Limanovskii, S.N. Denisenko, and S.G. Rassolov, *Mater. Sci. Eng. A* 323, 91 (2002).
44. T. Gheiratmand, H.R.M. Hosseini, P. Davami, F. Ostadhossein, M. Song, and M. Gjoka, *Nanoscale* 5, 7520 (2013).
45. A. Druker, P. La Roca, P. Vermaut, P. Ochin, and J. Mallarría, *Mater. Sci. Eng. A* 556, 936 (2012).
46. C. Chattopadhyay, A. Prasad, and B.S. Murty, *Acta Mater.* 153, 214 (2018).
47. M. Laurent-Brocq, L. Perrière, R. Pirès, F. Prima, P. Vermaut, and Y. Champion, *Mater. Sci. Eng. A* 696, 228 (2017).
48. F. Otto, N.L. Hanold, and E.P. George, *Intermetallics* 54, 39 (2014).
49. Y. Lin, B. Wu, S. Li, S. Mao, X. Liu, Y. Zhang, and L. Wang, *Mater. Sci. Eng. A* 621, 212 (2015).
50. Y. Lin, S. Mao, Z. Yan, Y. Zhang, and L. Wang, *J. Alloys Compd.* 651, 699 (2015).
51. D.J. Powell, R. Pilkington, and D.A. Miller, *Acta Metall.* 36, 713 (1988).
52. E. Ma, *JOM* 58, 49 (2006).

**Publisher's Note** Springer Nature remains neutral with regard to jurisdictional claims in published maps and institutional affiliations.